ACCSCIENCE PUBLISHING

Asian Journal of Water, Environment and Pollution

REVIEW ARTICLE

Insight into the bactericidal mechanisms of g-C3N4-based metal and metallic-compound junctions: A review

Mingjuan Zhang[1], Jingyi Zhao[1], Taotao Zeng[2], Chi Ma[3], Wenjing Xue[4], Jisui Tan[5], Hongbiao Cui[1]*, and Guodong Fang[6]*

[1]Anhui Province Engineering Research Center of Water and Soil Resources Comprehensive Utilization and Ecological Protection in High Groundwater Mining Area, Anhui University of Science and Technology, Huainan, Anhui, China

[2]Hunan Province Key Laboratory of Pollution Control and Resources Reuse Technology, University of South China, Hengyang, Hunan, China

[3]Key Laboratory of Food & Environment & Drug Monitoring and Testing of Universities in Hunan Province, Hunan Police Academy, Changsha, Hunan, China

[4]College of Environmental Science and Engineering, Yangzhou University, Yangzhou, Jiangsu, China

[5]Shenzhen Key Laboratory of Nano-Biosensing Technology, College of Chemistry and Environmental Engineering, Shenzhen University, Shenzhen, Guangdong, China

[6]State Key Laboratory of Soil and Sustainable Agriculture, Institute of Soil Science, Chinese Academy of Sciences, Nanjing, Jiangsu, China

***Corresponding authors:**
Hongbiao Cui
(cuihongbiao0554@163.com);
Guodong Fang
(gdfang@issas.ac.cn)

Citation: Zhang M, Zhao J, Zeng T, *et al.* Insight into the bactericidal mechanisms of g-C3N4-based metal and metallic-compound junctions: A review. *Asian J Water Environ Pollut.* 2026;23(3):026090051. doi: 10.36922/AJWEP026090051

Received: February 27, 2026

Revised: March 29, 2026

Accepted: April 2, 2026

Published online: May 18, 2026

Abstract

The use of sunlight to inactivate bacteria through photocatalysis is crucial for a sustainable future. Bactericidal performance is closely related to the charge dynamics of semiconductors. Among various semiconductors, graphitic carbon nitride (g-C_3N_4) has emerged as an attractive candidate for photocatalytic sterilization due to its chemical stability and versatility as a platform for constructing composites. However, the visible-light absorption and charge-separation performance of pristine g-C_3N_4 are insufficient, which limits further improvement in its bactericidal performance. Constructing g-C_3N_4-based metal or metallic-compound junctions has been shown to improve charge dynamics, including the introduction of plasma with surface plasmon resonance effect to photocatalysis and the construction of g-C_3N_4-based Schottky junctions. In this review, we first outline the basic principles of photocatalytic sterilization and then discuss the close relationship between bactericidal performance and the energy-band structure of semiconductors. We next summarize the factors limiting the performance of pristine g-C_3N_4, review common strategies for improving its bactericidal activity, and explain the underlying mechanisms. Finally, we discuss the remaining challenges and potential strategies to improve the practical applicability of g-C_3N_4-based metal and metallic-compound junctions.

Keywords: Photocatalytic sterilization; g-C_3N_4; Surface plasmon resonance effect; Schottky junction; Bactericidal mechanism

1. Introduction

The performance of photocatalytic sterilization is closely related to the charge dynamics of semiconductors, i.e., the generation, separation, and transfer of photogenerated charge carriers.[1] Since the discovery of bacterial inactivation by titanium dioxide (TiO_2) powders in 1985,[2] various semiconductors have been investigated for use in photocatalytic sterilization.[3] Considering that only a small portion of sunlight lies in the ultraviolet region of the solar spectrum (~4%), it is essential—from the standpoint of maximizing solar energy utilization and enhancing the generation of photogenerated electrons and holes—to employ semiconductors that respond to visible (Vis) light, which accounts for approximately 45% of the solar spectrum.[4] Graphitic carbon nitride (g-C_3N_4) is a non-metallic Vis light-responsive semiconductor. Owing to its readily available raw materials, tunable band gap (E_g), and adjustable morphology, it exhibits broad application prospects in photocatalytic sterilization.[5-7] However, the thermodynamic contradiction between the absorption of long-wavelength light and the high redox potentials of the photogenerated electrons and holes in pristine g-C_3N_4 is irreconcilable, which limits its bactericidal performance.[8] Integrating the plasma with the surface plasmon resonance (SPR) effect into photocatalysis is an effective strategy to optimize the charge generation dynamics; it can overcome the bandgap limitations of g-C_3N_4 and function through charge and energy transfer.[9] Many reviews have reported that the above strategy has greatly improved the bactericidal performance of the g-C_3N_4-based photocatalysts.[10,11] However, in most reviews on photocatalytic sterilization, researchers have focused on analyzing bacterial inactivation at the microscopic, molecular, and genetic levels.[12] In terms of the sterilization mechanism of the g-C_3N_4/plasma system, most studies have focused on plasma-induced charge transfer by injecting hot carriers into adjacent g-C_3N_4,[13] however, there are relatively few studies on the injection efficiency of hot carriers and whether plasma still functions through energy transfer. With regard to the sterilization mechanism of the g-C_3N_4-based Schottky junction, researchers have been dedicated to exploring the charge transfer of photocatalysts after being excited by light, while the charge transfer caused by the difference in Fermi levels (E_f) between g-C_3N_4 and another metal or metallic compound during the photocatalyst synthesis stage has rarely been a focus.[14] It is worth noting that the charge transfer in this process forms a built-in electric field, which is the driving force for the separation and directional transfer of photogenerated electrons and holes at the contact interface after the photocatalysts are excited by light. Meanwhile, less attention has been paid to the correspondence between the direction and strength of the built-in electric field and the E_f, and why the energy bands in the built-in electric field bend.

Accordingly, the current research bottlenecks in elucidating the bactericidal mechanism of g-C_3N_4-based metal or metallic-compound junctions are as follows:

(i) thermodynamic limitations: Pristine g-C_3N_4 exhibits an inherent contradiction between broad-spectrum light absorption and high redox capability, making it difficult for a single material system to simultaneously achieve efficient light absorption and robust charge carrier redox capacity;
(ii) insufficient understanding of the SPR effect mechanism: Existing reviews primarily focus on the role of plasmonic hot-carrier injection in promoting charge separation. However, they lack a systematic analysis of the synergistic mechanisms, hierarchy, and applicability of "charge transfer" versus "energy transfer" (such as localized electromagnetic field enhancement and resonant photon scattering) within the SPR effect. Notably, the energy transfer pathway has received insufficient attention;
(iii) incomplete understanding of interfacial charge processes in Schottky junction: Most studies concentrate solely on charge transfer under photoexcitation, neglecting the spontaneous interfacial charge transfer and the resulting built-in electric field that occurs during the synthesis stage of photocatalytic materials due to the E_f difference between g-C_3N_4 and metals/metal compounds. The decisive role of this built-in electric field in the separation and direct migration of photogenerated carriers, along with its direction/intensity in relation to the E_f and the physical nature of band bending, remains inadequately elucidated and distinguished.

In response to the above bottlenecks, the core innovations and contributions of this review are embodied in the following three aspects:

(i) Systematic analysis of the dual mechanisms by which the SPR effect regulates charge-generation dynamics. This review explicitly distinguishes between and systematically delineates the conditions, mechanisms, and synergistic effects of charge transfer and energy transfer pathways within the SPR effect. In particular, it provides an in-depth exposition of the energy transfer mechanism (localized electromagnetic field enhancement and resonant photon scattering), offering a theoretical foundation for the rational design of efficient plasmonic photocatalysts;
(ii) Distinguishing and clarifying the two key stages of charge transfer in the Schottky junction. This work explicitly distinguishes between two distinct yet closely

related charge transfer processes in the g-C_3N_4-based Schottky junctions: the "synthesis stage" (interfacial charge transfer and built-in electric field formation driven by the E_f difference) and the "photoexcitation stage" (built-in electric field-driven separation of photogenerated carriers). It elucidates the synergistic contributions of these two stages to photocatalytic sterilization performance;

(iii) Elucidating the intrinsic relationship between the direction/intensity of the built-in electric field and band bending. This review provides an in-depth explanation of how the direction and intensity of the built-in electric field are determined by the E_f difference between g-C_3N_4 and metals/metal compounds. Drawing on band theory, it explains the physical origin of interfacial band bending and its decisive role in carrier separation efficiency, thereby addressing a theoretical gap in previous reviews.

In this review, we outline the prerequisites for the SPR effect, including charge transfer and energy transfer. The mechanism of the SPR effect regulates the charge generation kinetics, i.e., the charge or energy transfer, or both, and the mechanism of energy transfer, i.e., local electromagnetic field enhancement or resonant photon scattering, or both/all of them. As far as the g-C_3N_4-based Schottky junction is concerned, two distinct charge transfer processes in the built-in electric field during the photocatalyst synthesis and photoexcitation stages are clearly distinguished. The correspondence between the direction/intensity of the built-in electric field and the E_f is explained. The reasons for the bending of the energy bands under a built-in electric field are explained. The two completely different driving forces that cause the separation and directional transfer of photogenerated electrons and holes have been clarified. Finally, challenges and improvement strategies for g-C_3N_4-based metal or metallic compound junctions are proposed to enhance their practical application potential in water disinfection.

2. The basic principle of photocatalytic sterilization

Photocatalytic sterilization stems from oxidative damage to bacteria caused by reactive oxygen species (ROS).[15] The process mainly involves four stages:

(i) The photocatalysts absorb light energy to produce electron–hole pairs,

(ii) These electron–hole pairs separate into electrons (e^-) and holes (h^+), which then migrate to the photocatalyst surface,

(iii) The e^- and h^+ react with oxygen (O_2) and water (H_2O) adsorbed on the surface of semiconductors to produce ROS. Specifically, O_2 is reduced by photogenerated electrons to generate superoxide radicals ($\cdot O_2^-$), which are further converted into hydrogen peroxide (H_2O_2), hydroxyl radicals adsorbed on the surface of photocatalysts ($\cdot OH_{ads}$), and singlet oxygen ($^1O_2$).[16–18] Meanwhile, the holes can oxidize H_2O and related intermediates to generate H_2O_2, $\cdot OH_{ads}$, and $^1O_2$.[19] It can be observed that both H_2O_2 and $\cdot OH_{ads}$ exhibit oxidation and reduction pathways. The formation paths of $\cdot O_2^-$, $^1O_2$, $\cdot OH_{ads}$, and H_2O_2 are shown in **Equations 1–10**. It is worth noting that different types of ROS exhibit distinct bactericidal properties due to differences in redox potential, lifetime, diffusion distance, and targeting specificity.[20] Hydroxyl radicals ($\cdot OH$) possess the highest oxidation potential (~ 2.8 V versus normal hydrogen electrode) and react non-selectively with almost all biomolecules (e.g., lipids, proteins, and DNA) at diffusion-limited rates, making them the most potent ROS for sterilization.[21] However, their extremely short lifetime (nanoseconds) limits their effective diffusion distance to only a few nanometers, confining their action to the vicinity of the photocatalyst surface.[22] In contrast, $\cdot O_2^-$ exhibits lower reactivity and longer lifetime (microseconds to milliseconds), enabling it to diffuse farther and exert indirect bactericidal effects through subsequent transformation into H_2O_2 or $\cdot OH$.[23] H_2O_2 is relatively stable (lifetime of minutes to hours) and can penetrate bacterial cell membranes to reach intracellular compartments, where it induces oxidative stress via Fenton or Haber–Weiss reactions to generate highly reactive $\cdot OH$ *in situ*. $^1O_2$, generated mainly via energy transfer, has a moderate lifetime (microseconds) and exhibits selective reactivity toward electron-rich biomolecules such as unsaturated lipids and amino acid residues, contributing to membrane damage.[24] These distinct characteristics determine the dominant sterilization pathways under different photocatalytic systems and reaction conditions, and thus the rational design of photocatalysts should consider the targeted generation of specific ROS based on the physiological features of target microorganisms.[25]

The reduction path for the generation of $\cdot O_2^-$

$$O_2 + e^- \rightarrow \cdot O_2^- \quad (1)$$

The oxidation path for the generation of H_2O_2

$$h^+ + H_2O_{ads} \rightarrow \cdot OH_{ads} + H^+ \quad (2)$$

$$\cdot OH_{ads} + \cdot OH_{ads} \rightarrow H_2O_2 \quad (3)$$

The reduction path for the generation of H_2O_2

$$H_2O + \cdot O_2^- \rightarrow \cdot OOH + OH^- \quad (4)$$

$$2 \cdot OOH \rightarrow O_2 + H_2O_2 \quad (5)$$

The oxidation path for the generation of $\cdot OH_{ads}$

$$h^+ + H2O_{ads} \rightarrow \cdot OH_{ads} + H^+ \quad (6)$$

The reduction path for the generation of $\cdot OH_{ads}$

$$\cdot O_2^- + 2H^+ + e\text{-} \rightarrow H_2O_2 \quad (7)$$

$$H_2O_2 + \cdot e\text{-} \rightarrow \cdot OH + OH^- \quad (8)$$

The oxidation path for the generation of $^1O_2$

$$h^+ + \cdot O_2^- \rightarrow {}^1O_2 \quad (9)$$

$$\cdot O_2^- - e^- \text{-} \rightarrow {}^1O_2 \quad (10)$$

(iv) The h^+, e^-, $^1O_2$, $\cdot O_2^-$, and $\cdot OH_{ads}$ species attack bacteria adsorbed on the photocatalyst surface.[26] In the meantime, the H_2O_2 and ·OH diffuse into the solution ($\cdot OH_{bulk}$) and attack the bacteria in solution.[27] The dominant ROS involved in sterilization vary with the type of photocatalyst and reaction conditions. For instance, Sun *et al.*[28] constructed a photoelectrocatalytic system using a TiO_2 nanotube array as the photoanode and UV light as the light source to inactivate *Escherichia coli K-12*. In this system, H_2O_2 is considered the dominant ROS, which can cross the bacterial cell membrane and produce ·OH with greater reactivity via the Haber–Weiss or Fenton reaction. Meanwhile, the bacterial cell can continuously produce $\cdot O_2^-$ through aerobic respiration. The sterilization mechanism is shown in Figure 1. In the initial stage, the increased ROS levels of H_2O_2, ·OH, and $\cdot O_2^-$ in the bacterial cell are partially quenched by antioxidant enzymes such as catalase and superoxide dismutase, which can catalyze the transformation and detoxification of H_2O_2 and $\cdot O_2^-$. However, as ROS is continuously produced in the bacterial cell, antioxidant enzymes become inactivated. Then, ROS attacks the bacterial cell wall, causing the loss of cell membrane integrity and increased permeability. As the reaction progresses, the bacterial cell membrane ruptures, releasing cellular proteins and nucleic acids. Finally, the released cellular components are further degraded and mineralized over a prolonged reaction time.[29–31]

It can be seen that the efficiency of ROS attacks bacteria mainly depends on the following four key continuous processes:

(i) The generation of electron–hole pairs,
(ii) The separation of electron–hole pairs,
(iii) The formation of ROS,
(iv) The attack of ROS on bacteria.

These four key continuous processes are indispensable, and only when all of them are completed with optimal efficiency can the overall photocatalytic performance be optimized. Notably, these four key continuous processes are closely related to the energy-band structures of photocatalysts, which determine light absorption, electron-hole pair separation, and the redox potentials of electrons and holes.[32,33] Therefore, the energy-band structure of a photocatalyst influences ROS formation and bacterial attack. Consequently, the design and development of efficient photocatalysts are key to improving the efficiency of photocatalytic sterilization.

3. The construction of g-C_3N_4-based composite materials

The g-C_3N_4, as a non-metallic polymer semiconductor, offers key advantages over traditional metal-based catalysts: low cost, simple synthesis, excellent chemical and thermal stability, and the absence of precious or heavy metals, thereby avoiding the risk of secondary pollution.[34] Its unique two-dimensional layered structure endows it with a large specific surface area and abundant active sites, while its moderate bandgap (~ 2.7 eV) enables effective response to Vis light, demonstrating significant potential for sustainable solar-driven catalysis.[35] In environmental applications, g-C_3N_4 primarily plays three roles. First, photocatalytic degradation of organic pollutants efficiently degrades dyes, antibiotics, and endocrine-disrupting chemicals in water by generating ROS.[36] Second, photocatalytic reduction in environmental remediation, reducing toxic heavy metals such as hexavalent chromium to less toxic forms, or converting CO_2 into fuels like methane, thereby achieving synergistic pollution reduction and carbon mitigation.[37] Third, air purification by catalytically oxidizing nitrogen oxides and volatile organic compounds. Additionally, leveraging its good biocompatibility, g-C_3N_4 can be used to construct antibacterial materials for controlling waterborne pathogens.[38] With its comprehensive advantages of low cost, environmental friendliness, and Vis light responsiveness, g-C_3N_4 has emerged as a highly promising non-metallic alternative material in the field of environmental catalysis.

Semiconductors have unique energy-band structures, e.g., the conduction band potential (E_{CB}), the valence band potential (E_{VB}), E_g, E_f, and the work functions (W_s), which endow them with different light absorption properties, redox potential, as well as the separation and transfer

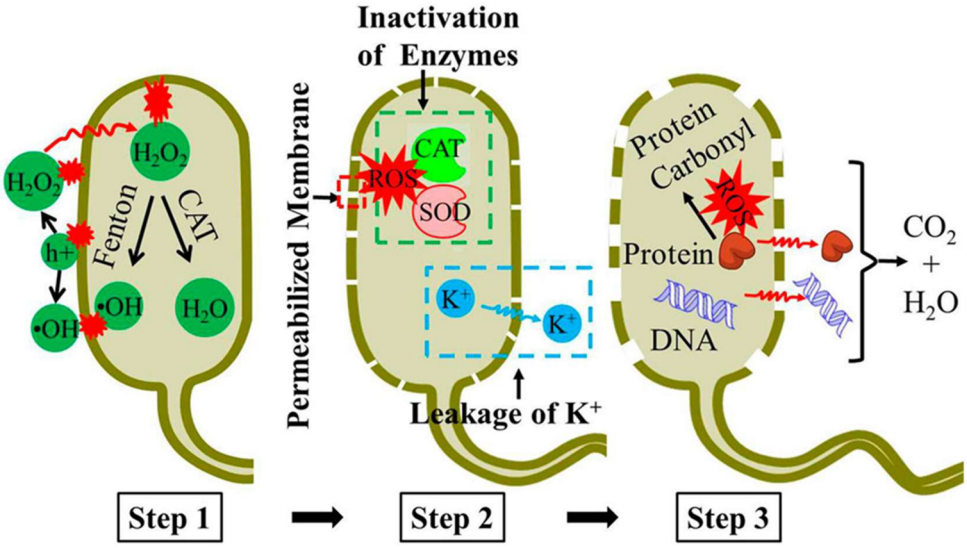

Figure 1. The mechanisms involved in the inactivation of *E. coli K-12* during the photo-electrocatalytic processes. Reproduced with permission from Ref.[28] Copyright 2014 American Chemical Society.
Abbreviations: CAT: Catalase; CO_2: Carbon dioxide; h^+: Photogenerated hole; H_2O: Water; H_2O_2: Hydrogen peroxide; K^+: Potassium; ·OH: Hydroxyl radical; ROS: Reactive oxygen species; SOD: Superoxide dismutase.

capabilities of electrons and holes. As a consequence, the construction of g-C_3N_4-based semiconductor composite can synergistically leverage the structural advantages of both.[39,40] For example, if another semiconductor also responds to Vis light, the resulting semiconductor composite shows enhanced Vis light absorption, thereby inducing the production of more electron–hole pairs.[41] Furthermore, when the energy-band structure of g-C_3N_4 and another semiconductor is matched, the built-in electric field created by the energy-band structure alignment of the two semiconductors leads to the transfer of electrons and holes directionally.[42] Therefore, the separation efficiency of electrons and holes in the g-C_3N_4-based semiconductor composite is significantly improved, which can be measured by the photo-electrochemical characterization, e.g., electrochemical impedance spectroscopy, photoluminescence emission spectra, and the transient photocurrent responses spectra (i–t).[43] Based on the type of energy-band structure alignment, g-C_3N_4-based composites that optimize the photocatalytic performance of g-C_3N_4 are commonly classified into five types:[44]

(i) The type II heterojunction (Figure 2A),
(ii) The Z-scheme heterojunction (Figure 2B) and homojunction,
(iii) The intramolecular donor–acceptor-like p–n homojunction,
(iv) The Schottky junction (Figure 2C),
(v) The introduction of plasma with the SPR effect (Figure 2D).

In addition, the construction of a metal or metallic compound junction is another effective method to improve the photocatalytic performance of g-C_3N_4. The metals have excellent electrical conductivity and high activation energy for redox reactions. Precious metals, e.g., gold (Au), silver (Ag), copper (Cu), as well as certain metallic compounds, exhibit strong SPR effects, with plasmonic bands located in the Vis or near-infrared (NIR) regions.[45] The construction of g-C_3N_4-based metal or metallic-compound junctions includes a Schottky junction and the introduction of precious metals or metallic compounds with the SPR effect.

The rational selection of a secondary component to couple with g-C_3N_4 is governed by three fundamental principles:

(i) Energy band alignment: the band structures (i.e., E_{CB}, E_{VB}, and work function [W_f]) of the secondary material must be compatible with those of g-C_3N_4 to form the desired charge transfer pathway (e.g., type-II, Z-scheme, or Schottky junction).[46] The band-edge positions determine the thermodynamic driving force for the migration of photogenerated electrons and holes, as well as the redox potential of the separated charge carriers.[47,48]
(ii) Spectral response compatibility: to maximize solar energy utilization, the secondary component should ideally possess a band gap that complements g-C_3N_4. For Vis-light-active semiconductors, the combination can broaden the overall light absorption range.[49] For wide-bandgap semiconductors, they may serve as

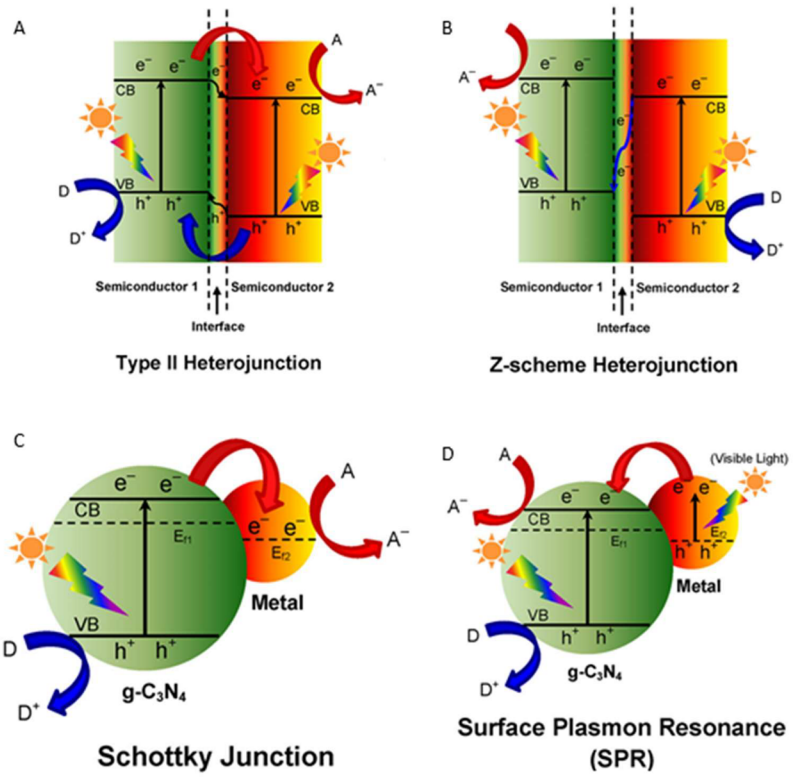

Figure 2. The g-C3N4-based composite. (A) The type II heterojunction. (B) The Z-scheme heterojunction. (C) Schottky junction. (D) The surface plasmon resonance effect. Reproduced with permission from Ref.[44] Copyright 2016 American Chemical Society.
Abbreviations: CB: Conduction band; D: Deuterium; D^+: Deuteron; e^- : Electron; E_f: Fermi levels; h^+: Photogenerated hole; VB: Valence band.

electron transport mediators. For plasmonic materials (e.g., Au, Ag), their SPR should overlap with the absorption range of g-C_3N_4 to enable hot-electron injection.[50]

(iii) Interfacial lattice matching and chemical compatibility: a low lattice mismatch and strong chemical interaction at the heterojunction interface facilitate the formation of a high-quality contact, which minimizes interfacial defects and provides a low-resistance pathway for charge carrier transfer.[51]

The photocatalytic performance of g-C_3N_4-based composites is highly dependent on the precise control of structural parameters, which can be regulated according to the following rules:

(i) Morphology and dimensionality: the morphology of both g-C_3N_4 (e.g., nanosheets, nanotubes, or mesoporous structures) and the secondary component (e.g., nanoparticles, nanorods, or two-dimensional layers) dictates the contact area and charge transfer distance.[52] Optimizing the dimensionality, such as constructing two-dimensional/two-dimensional interfaces, maximizes the interfacial contact area and shortens the bulk-to-surface migration distance of charge carriers, thereby promoting efficient spatial charge separation.[53]

(ii) Interface engineering: the quality of the heterojunction interface is critical. Atomic-level contact, often achieved via *in situ* growth or surface functionalization, reduces interfacial resistance and enhances the built-in electric field strength.[54] The presence of an intermediate layer (e.g., carbon dots or conductive polymers) can further modulate the interfacial barrier and act as a solid-state electron mediator, particularly in all-solid-state Z-scheme systems.[55]

(iii) Component proportion and distribution: the mass ratio between g-C_3N_4 and the secondary component determines the balance between light absorption, surface active sites, and charge separation efficiency.[56] Excessive loading of the secondary component may lead to the "shielding effect", reducing light penetration to the g-C_3N_4 surface, while insufficient loading results in inadequate heterojunction interfaces.[57] Uniform dispersion of the secondary component on

the g-C_3N_4 matrix is essential to avoid the formation of recombination centers.

(iv) Crystallinity and defect control: the crystallinity of the secondary semiconductor influences its charge mobility, while the introduction of controlled defects (e.g., nitrogen vacancies in g-C_3N_4) can tune its band structure and act as active sites.[58] However, excessive defects may serve as recombination centers, necessitating precise regulation through thermal treatment or chemical doping.[59]

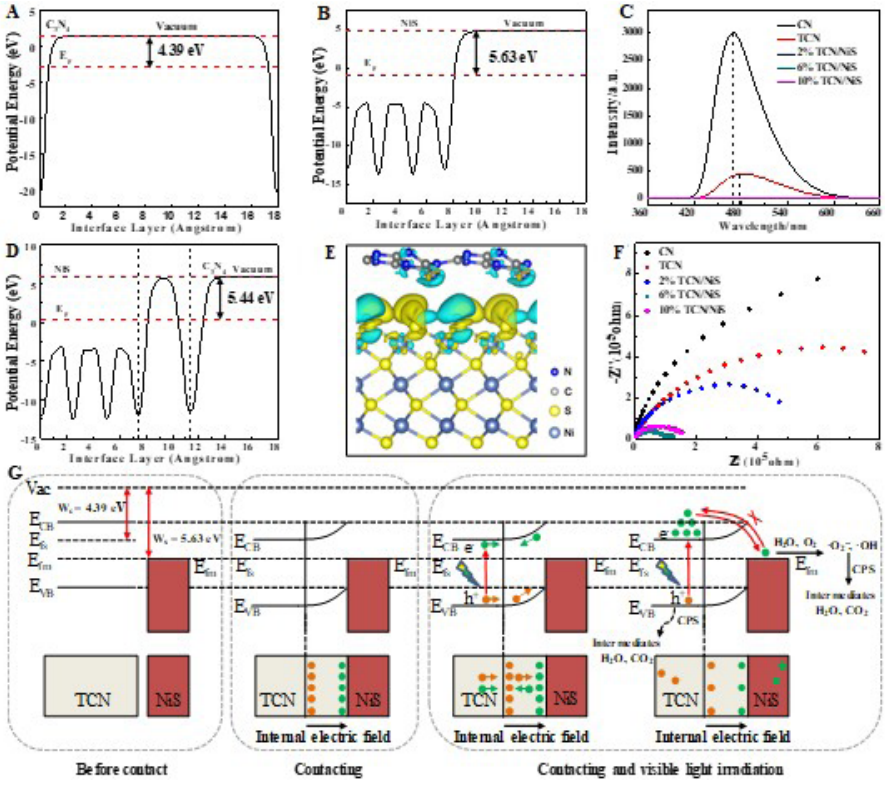

Figure 3. The work function of (A) TCN, (B) NiS, (C) TCN/NiS heterojunction, (D) charge density difference of TCN/NiS, (E) photoluminescence (PL) spectra, (F) electrochemical impedance spectroscopy (EIS) of the photocatalysts, and (G) the unidirectional electron transfer in TCN/NiS. Reproduced with permission from Ref.[60] Copyright 2021 Elsevier.

Abbreviations: CO_2: Carbon dioxide; CN: graphitic carbon nitride;; e^-: Electron; E_{CB}: Conduction band potential; E_{fm}: Fermi level of the metal; E_{fs}: Surface Fermi level; E_{VB}: Valence band potential; h^+: Photogenerated hole; H_2O_2: Hydrogen peroxide; NiS: nickel sulfide; O_2: Oxygen; $\cdot O_2^-$: Superoxide radical; ·OH: Hydroxyl radical; TCN: tubular graphitic carbon nitride; Wc: Work function of the conduction-related material; Ws: Work function of surface layer.

3.1. The g-C_3N_4-based Schottky junction

The construction of the g-C_3N_4-based Schottky junction should meet the following two requirements:[61]

(i) The g-C_3N_4 is in contact with a metal or a metallic compound directly,

(ii) The W_s of g-C_3N_4 should be less than that of a metal or metallic compound (W_m).

In our previous work, a Schottky junction of three-dimensional tubular g-C_3N_4/flowerlike nickel sulfide (TCN/NiS) was constructed.[60] The W_f of TCN is lower than that of NiS (Figure 3A,B). When g-C_3N_4 is combined with NiS ($W_s < W_m$), electrons of g-C_3N_4 transfer to NiS to balance the potential difference between W_s and W_m. The above electron transfer process causes upward band bending in the g-C_3N_4 energy band and the formation of a Schottky junction (Figure 3C,D). It is important to emphasize that the formation of a Schottky junction is independent of illumination. As shown in Figure 3G, the g-C_3N_4 in the Schottky junction is excited, and the electrons transfer from the E_{VB} to E_{CB} under Vis light irradiation. Subsequently, the electrons in the E_{CB} of g-C_3N_4 transfer to NiS under the influence of the built-in electric field. Due to the existence of a Schottky junction, the electrons that have been transferred to NiS cannot return to the E_{CB} of g-C_3N_4. Thus, the construction of a Schottky junction

with unidirectional electron transfer properties effectively separates the electrons and holes of g-C_3N_4 (Figure 3E,F). The electrons in NiS participate in the subsequent reduction reaction, while the holes remaining in g-C_3N_4 participate in the subsequent oxidation reaction. Guo *et al.*[62] use TCN/hydroxyl-terminated titanium carbide (Ti_3C_2) MXene (TC(OH)) as a model case to further clarify the relationship between Schottky barrier height (SBH) and photocatalytic sterilization efficiency (Figure 4). The reduction of SBH in TC(OH) promotes the rapid transfer of photogenerated electrons from TCN to TC(OH), and shifts the O_2 reduction pathway toward a one-step two-electron process. The transformation of the O_2 reduction pathway generates more selective, dominant bactericidal ROS, such as H_2O_2, thereby enhancing the bactericidal efficiency in the water environment.

3.2. The introduction of plasma with the surface plasmon resonance effect

As mentioned earlier, there is an irreconcilable contradiction between the long-wavelength light absorption and the high redox potential of photogenerated electrons and holes in the single-component semiconductors. This dilemma could be addressed by introducing plasma (precious metals or metallic compounds) to exploit the SPR effect.[63] When a plasma is irradiated with light whose frequency matches the natural frequency at which its surface free electrons oscillate against the restoring force of the positive nuclei, resonance occurs. This generates intense, highly localized electromagnetic fields. This collective oscillation of free electrons is known as the SPR effect.[64] Generally, the SPR effect is strongly dependent on the size and morphology of the nanoparticles.[65] It is reported that 50 nm titanium nitride (TiN) nanoparticles exhibit higher absorption efficiency and hot-electron generation than 20 nm nanoparticles. In addition, the cubic geometry of TiN nanoparticles contributes to strong field enhancement via hot spots at their vertices[66]. In terms of the plasma with the SPR effect under light irradiation, if the energy of the incident light satisfies **Equation 11**, it can excite the plasma to generate hot carriers (hot electrons and holes).[67]

$$h\nu \geq E_{CB} - E_f \quad (11)$$

where hν is the energy of the incident light, E_{CB} is the conduction band potential of the semiconductor, and E_F is the Fermi level of the plasma.

It can be noticed that the energy required to excite the plasma is much lower than that required to excite the semiconductor (hν ≥ band gap energy).[68] When the plasma with the SPR effect comes into contact with a semiconductor directly, the hot carriers with energy greater than the SBH generated by the plasma can be injected into the adjacent semiconductor.[69] Specifically, with regard to the n-type semiconductor, e.g., g-C_3N_4, the hot electrons are injected into the E_{CB}, which participates in the subsequent reduction

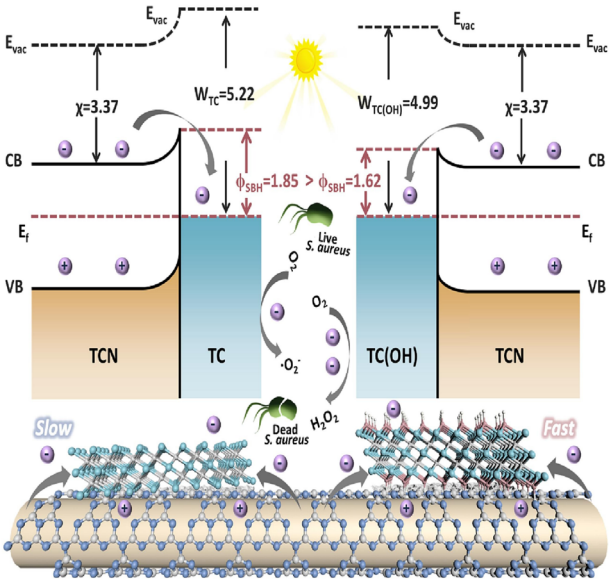

Figure 4. The photocatalytic disinfection mechanism in TCN/TC(OH)-3. Reproduced with permission from Ref.[62] Copyright 2023 Elsevier.
Abbreviations: CB: Conduction band; E_f: Fermi level; E_{vac}: vacuum level; H_2O_2: Hydrogen peroxide; ΦSBH = Schottky barrier height; TC: Titanium carbide; TCN: Tubular graphitic carbon nitride (g-C_3N_4); TC(OH): Hydroxyl-terminated titanium carbide; VB: Valence band; W: Work function; χ: Electron affinity.

reaction (Figure 5A). Injection efficiency is closely related to the density of states in the plasma and the SBH at the interface between the plasma and the semiconductor.[70] The low-density states near E_f and the low W_m in plasma reduce the chance of hot electrons backscattering after injection, thereby enhancing the injection efficiency. Conversely, the hot holes are injected into the E_{VB} of a p-type semiconductor for participating in the subsequent oxidation reaction (Figure 5B). The injection of hot carriers from plasma into an adjacent semiconductor can be intuitively verified using finite element method (FEM) calculations. For example, the cuprous oxide (Cu_2O) and Ag nanoparticles are combined with nitrogen-vacancy g-C_3N_4 (Cu_2O/Ag/V-CN) and used for photocatalytic sterilization.[55] The FEM calculations verify that the hot holes produced by plasma Ag are injected into the p-type semiconductor Cu_2O (Figure 6A,F), and the bactericidal efficiency is shown in Figure 6G,H. Notably, the injected hot electrons or hot holes are capable of maintaining the same redox potential as the photogenerated electrons in the E_{CB} of g-C_3N_4 or the photogenerated holes in the E_{VB} of a p-type semiconductor, even if the semiconductors cannot be excited by the lower-energy incident light sources, e.g., Vis or NIR light.[71]

In addition to injecting hot carriers (charge transfer), the SPR effect of plasma can also function through energy transfer, i.e., the local electromagnetic field enhancement (Figure 6I) and resonant photon scattering (Figure 6J) by promoting the generation of photogenerated charge carriers in the adjacent semiconductor, e.g., g-C_3N_4.[72] The energy transfer occurs only when the spectral range of the incident light sources covers the absorption band of semiconductor and the SPR band of the plasma, considering that both semiconductor and plasma are needed to absorb incident light.[73] In view of this, if the spectral range of the incident light only covers the SPR band of the plasma but not the absorption band of the semiconductor, the energy transfer of the plasma and the bandgap excitation of the semiconductor can be excluded, and the charge transfer of the plasma can be studied exclusively. Furthermore, the energy transfer of resonant photon scattering occurs only when the absorption band of the semiconductor overlaps with the SPR band of the plasma.[64]

The specific roles of plasma were investigated by comparing the transient photocurrent intensities in different spectral ranges ($\lambda > 550$ nm and $\lambda > 420$ nm), taking the phosphorus-doped fiber tubular g-C_3N_4/g-C_3N_4/titanium nitride (FCN/CN/TiN) as a model case.[74] The SPR band of TiN is located 500~800 nm, while the absorption band of FCN/CN is less than 470 nm. The photocurrents in FCN/CN/TiN ($\lambda > 550$ nm) originated from the hot electron injection from TiN to FCN, and that in FCN/CN ($\lambda > 420$ nm) derived from the photogenerated electrons generated by the bandgap excitation of FCN/CN. The photocurrent intensities in FCN/CN/TiN ($\lambda > 420$ nm) are larger than the sum of those in FCN/CN ($\lambda > 420$ nm) and

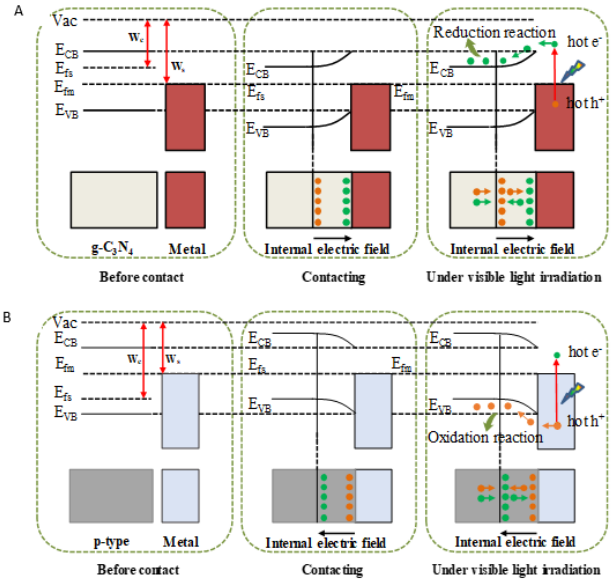

Figure 5. The charge transfer driven by the surface plasmon resonance effect in hybrid structures comprising (A) a metal and g-C_3N_4 junction and (B) a p-type semiconductor.
Abbreviations: e^-: Electron; E_{CB}: Conduction band potential; E_{fm}: Fermi level of the metal; E_{fs}: Fermi level of the semiconductor; E_{VB}: Valence band potential; h^+: Photogenerated hole; V_{ac}: Vacuum level; W_c: Conduction-band-related energy difference; W_s: Work function of the semiconductor.

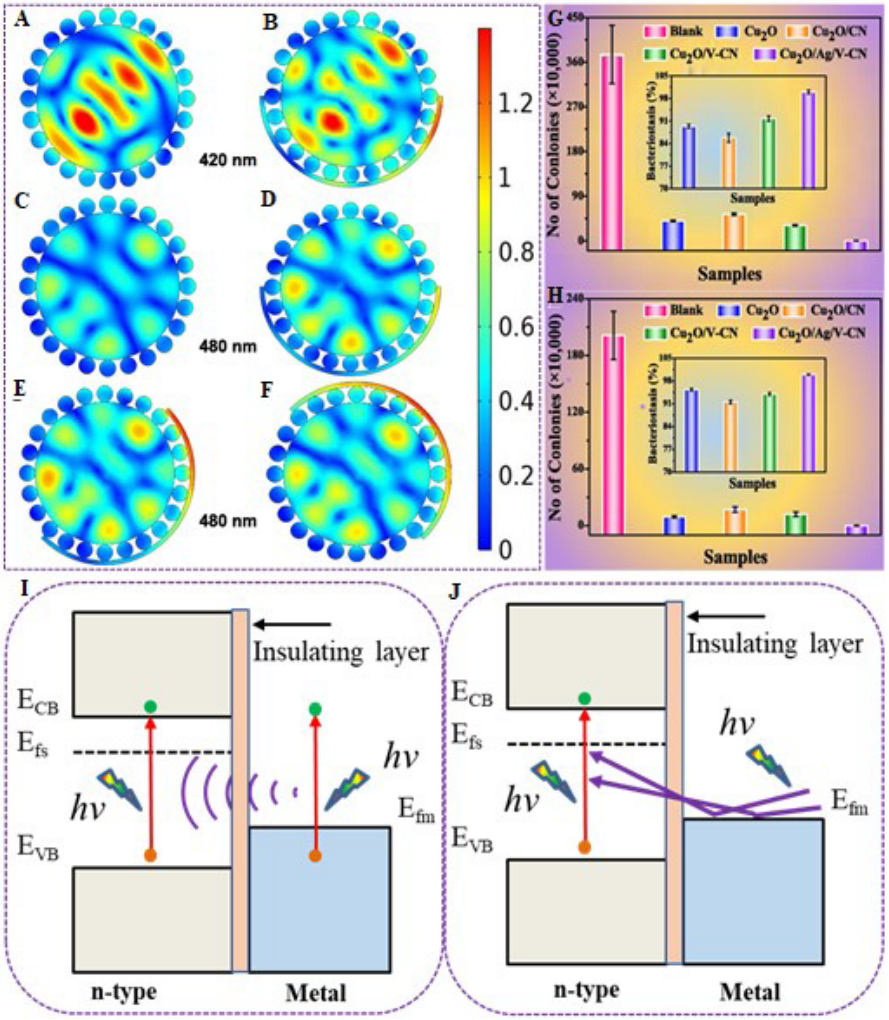

Figure 6. The FEM calculations of Cu_2O/Ag (a, c) and Cu_2O/Ag/V-CN (b, d–f) with incident light irradiated at 420 nm (A–B) and 480 nm (C–F). (G–H) Histogram of bacteriostatic data of different systems. Reproduced with permission from Ref.[55] Copyright 2022 Elsevier. The energy transfer mediated by the local electromagnetic field enhancement (I) and resonance photon scattering (J).

Abbreviations: Cu_2O: Cuprous oxide; Cu_2O/CN: Cuprous oxide/graphitic carbon nitride; Cu_2O/V-CN: Cuprous oxide/nitrogen-vacancy–rich g-C_3N_4; Cu_2O/Ag/V-CN: cuprous oxide/silver/vacancy-engineered graphitic carbon nitride; E_{CB}: Conduction band potential; E_{fm}: Fermi level of the metal; E_{fs}: Fermi level of the semiconductor; E_{VB}: Valence band potential; FEM: Finite element method; *hv*: Photon energy.

FCN/CN/TiN (λ > 550 nm), indicating that the plasma TiN does not involve charge transfer but energy transfer. Meanwhile, because the absorption band of FCN/CN does not overlap with the SPR band of TiN, the energy transfer of TiN is the local electromagnetic field enhancement rather than resonant photon scattering. Clarifying the specific roles of plasma enables targeted amplification of its effects to improve charge-generation kinetics. For example, the plasma bands of Au nanorods are extended from the Vis to NIR light region by adjusting the aspect ratio and overall size, which is conducive to making full use of sunlight to generate more hot electrons for injection into the adjacent g-C_3N_4.[75]

4. Conclusion and outlook

Bactericidal performance is closely related to semiconductor charge dynamics. This review clarifies the common strategies for optimizing the bactericidal performance of g-C_3N_4-based photocatalysts and discusses the underlying optimization mechanisms from the perspectives of energy-band structure and charge transport. In terms of the charge dynamics, we elaborate on the following three points:

(i) The direct contact between g-C_3N_4 and plasma is a prerequisite for injecting hot carriers, and FEM calculations can be used to verify the injection of hot carriers intuitively. The injection efficiency of hot

carriers is closely related to the density of states in the plasma and the SBH at the interface between the plasma and the semiconductor.

(i) In a g-C_3N_4/plasma system, in addition to injecting hot carriers into adjacent g-C_3N_4, the plasma might also function through energy transfer. The specific roles of plasma can be investigated by comparing transient photocurrent intensities across different spectral ranges, thereby enabling targeted amplification of its effects on charge-generation dynamics.

(ii) The improvement in the efficiency of separation and transfer is attributed to two distinct driving forces, i.e., the built-in electric field and the potential difference of E_{CB} and E_{VB} between the two semiconductors.

Although significant progress has been made in optimizing bactericidal performance, further work is needed to improve the practical applicability of g-C_3N_4-based photocatalysts:

(i) Environmentally relevant evaluation: emphasizing the need to simulate real-world conditions (e.g., using natural sunlight, considering the impact of natural organic matter, anions, and diurnal light intensity variations) to better assess true photocatalytic sterilization performance.

(ii) Integration with advanced oxidation processes: highlighting the synergistic potential of coupling photocatalysis with persulfate-based advanced oxidation processes, detailing how this combination enhances bactericidal efficacy through complementary reactive species and improves charge separation, while also addressing the effects of coexisting substances in real water matrices.

(iii) Development of immobilization techniques: proposing a shift from powdered catalysts to immobilized systems to overcome practical hurdles such as catalyst recovery, reaction control, and process standardization, thereby facilitating the transition from laboratory research to field-scale applications.

Acknowledgments

None.

Funding

This study was supported by the Scientific Research Foundation for High-level Talents of Anhui University of Science and Technology (2023yjrc121), Anhui Province Engineering Research Center of Water and Soil Resources Comprehensive Utilization and Ecological Protection in High Groundwater Mining Area (2024-WSREPMA-06), the Xizang Autonomous Region Key Research and Development Program (XZ202601ZY0192), the Scientific Foundation for Youth Scholars of Shenzhen University (868-000001032909), the Scientific Research Fund of Hunan Provincial Education Department (25B0912).

Conflict of interest

The authors declare that they have no competing interests.

Author contributions

Conceptualization: Mingjuan Zhang
Data curation: Mingjuan Zhang, Jingyi Zhao, Taotao Zeng, Hongbiao Cui,
Guodong Fang
Formal analysis: Hongbiao Cui, Guodong Fang
Funding acquisition: Mingjuan Zhang, Chi Ma, Jisui Tan
Project administration: Hongbiao Cui, Guodong Fang
Supervision: Jingyi Zhao, Taotao Zeng, Wenjing Xue
Writing – original draft: Mingjuan Zhang
Writing – review & editing: Jingyi Zhao, Taotao Zeng, Chi Ma, Wenjing Xue, Jisui Tan

Availability of data

Not applicable.

References

1. Chen H, Gao S, Huang G, Chen Q, Gao Y, Bi J. Built-in electric field mediated S-scheme charge migration in COF/In2S3 heterojunction for boosting H2O2 photosynthesis and sterilization. *Appl Catal B Environ.* 2023;343:123545.

doi: 10.1016/j.apcatb.2023.123545

2. Matsunaga T, Tomoda R, Nakajima T, Wake H. Photoelectrochemical sterilization of microbial cells by semiconductor powders. *FEMS Microbiol Lett.* 1985;29(1-2):211-214.

doi: 10.1111/j.1574-6968.1985.tb00864.x

3. Li R, Chen T, Pan X. Metal–organic-framework-based materials for antimicrobial applications. *ACS Nano*. 2021;15(3):3808-3848.

doi: 10.1021/acsnano.0c09617

4. Meng L, Zhao C, Zhang X, *et al.* Piezo-photocatalytic synergetic for H2O2 generation via dual-pathway over Z-scheme ZIF-L/g-C3N4 heterojunction. *Nano Energy*. 2024;128:109795.

doi: 10.1016/j.nanoen.2024.109795

5. Song J, Li C, Zhang X, Ma P, Zheng K. Hydrogen Peroxide Production with Photocatalysts Based on Carbon Nitride: Evaluation Criteria, Reaction Mechanism, Improvement Scheme, and Development Opportunity. *ACS Catal.* 2025;15(11):9058-9088.

doi: 10.1021/acscatal.5c01609

6. Qian X, Li W, Wang X *et al.* Multifunctional roles

of ionic microenvironments in the preparation, modification, and application of g-C3N4. *Adv Funct Mater.* 2025;35(11):2416946.

doi: 10.1002/adfm.202416946

7. Zhou T, Deng J, Chu Y, *et al.* Breaking the activity-selectivity trade-off through engineered scalable production of sulfur vacancy-rich pyrite for zero-oxidant targeted enrofloxacin removal. *Appl Catal B Environ.* 2025;381:125892.

doi: 10.1016/j.apcatb.2025.125892

8. Xiao T, Diao P. Quantifying localized surface plasmon resonance induced enhancement on metal@ Cu2O composites for photoelectrochemical water splitting. *Adv Mater.* 2025;37(28):2501069.

doi: 10.1002/adma.202501069

9. Ruan X, Ding C, Leng J *et al.* Decoupling of Carrier Pathways in Au/Cu-Zn3In2S6 Through Bulk Hole Trapping and Surface Hot Electron Accumulation Enhances Photocatalytic Hydrogen Peroxide Production. *Adv Mater.* 2025;37(44):e11422.

doi: 10.1002/adma.202511422

10. Ding Y, Yang G, Zheng S *et al.* Advanced photocatalytic disinfection mechanisms and their challenges. *J Environ Manag.* 2024;366:121875.

doi: 10.1016/j.jenvman.2024.121875

11. Ding Y, Wang C, Pei L *et al.* Emerging heterostructured C 3 N 4 photocatalysts for photocatalytic environmental pollutant elimination and sterilization. *Inorg Chem Front*. 2023;10(13):3756-3780.

doi: 10.1039/D3QI00657C

12. Zeng J, Li Z, Jiang H, Wang X. Progress on photocatalytic semiconductor hybrids for bacterial inactivation. *Mater Horiz.* 2021;8(11):2964-3008.

doi: 10.1039/D1MH00773D

13. She P, Li S, Li X, Rao H, Men X, Qin JS. Photocatalytic antibacterial agents based on inorganic semiconductor nanomaterials: a review. *Nanoscale*. 2024;16(10):4961-4973.

doi: 10.1039/D3NR06531F

14. Zhang X, Zhang S, Mathivanan K *et al.* Research progress and prospects in antifouling performance of photocatalytic sterilization: A review. *J Mater Sci Technol.* 2025;208:189-201.

doi: 10.1016/j.jmst.2024.04.052

15. Cong S, Zhou S, You J, Wang L, Wang X. Directionally Designed Double Z-Scheme Heterojunction: BiOBr and Carbon Dots-Reduced TiO2− x for Targeted Photocarriers Separation in Photocatalytic Sterilization. *Small*. 2025;21(37):e05905.

doi: 10.1002/smll.20 2505905

16. Ren X, Feng M, Mao M *et al.* Cyanobacteria for environmental, energy and biomedical application: a review. *Environ Chem Lett.* 2025;23(2):491-515.

doi: 10.1007/s10311-024-01814-3

17. Lu H, Zou F, Liu X, *et al.* Z-scheme g-C3N4/α-FOD heterojunction-assisted persulfate activation for degradation of tetracycline hydrochloride under visible light: Insights into mechanism. *Chem Eng J.* 2023;479:147224.

doi: 10.1016/j.cej.2023.147224

18. Liu X, Xiang T, Liu J, *et al.* AG single atoms boosting water dissociation on CU nanowires for efficient H * -Mediated nitrate reduction at Ultra-Low concentrations with ammonia recovery. *Adv Funct Mater.* 2025;36(15).

doi: 10.1002/adfm.202521402

19. Wu Q, Zheng G, Li L, Wang L. Enhancing Peroxidase-Like activity and photothermal property of Copper Single-Atom nanozyme via a cascade competition strategy. *Adv Funct Mater.* 2025;35(22).

doi: 10.1002/adfm.202422588

20. Jiang Z, Yue Q, Guo C, Lin H. Z-scheme CuBi2O4/carbon dots nanoflowers heterojunction to enhance solar photocatalytic sterilization. *Carbon*. 2025;241:120395.

doi: 10.1016/j.carbon.2025.120395

21. Jiang X, Hu J, Qin Y, *et al.* Novel dual bactericidal mechanism of TiO2 'solution' during photocatalytic sterilization. *Appl Surf Sci.* 2025;688:162409.

doi: 10.1016/j.apsusc.2025.162409

22. Yang YL, Wang CY, Wang NB *et al.* Ohmic-junction of Ag cluster decorated BiO2-x with strong built-in electric field enables efficient photocatalytic sterilization: DFT and mechanism insights. *Rare Met*. 2025;44(11):8680-8690.

doi: 10.1007/s12598-025-03405-9

23. Qiu L, Zhang Y, Wu B, *et al.* State-selective engineering in luminescent metal-organic frameworks: Ligand-to-ligand charge transfer activates superior photocatalytic sterilization in Wei River. *J Hazard Mater.*2025;500:140448.

doi: 10.1016/j.jhazmat.2025.140448

24. Fan Y, Liu J, Han X. Important contributions of in-situ produced H2O2 during photocatalytic sterilization of air by self-doped Bi2.15WO6. *Sep Purif Technol.* 2025;363:132052.

doi: 10.1016/j.seppur.2025.132052

25. Ren J, Luo X, Gao J, Fang X, An X, Chen Y. Rapid preparation of porous composite hydrogels developed via an activation-induced strategy for efficient solar steam generation and photocatalytic sterilization. *Sep Purif Technol.* 2025;382:136152.

doi: 10.1016/j.seppur.2025.136152

26. Wang W, Yu Y, An T, *et al.* Visible-Light-Driven

Photocatalytic Inactivation of E. coli K-12 by Bismuth Vanadate Nanotubes: Bactericidal Performance and Mechanism. *Environ Sci Technol.* 2012;46(8):4599-4606.

doi: 10.1021/es2042977

27. Qian G, Deng R, Liu X, *et al.* Achieving high carrier mobility of FE-ZNO and CU-ZNO laminated homo-junction nanofilm for rapid and highly effective photocatalytic sterilization. *Small*. 2025;21(35):e2503536.

doi: 10.1002/smll.202503536

28. Sun H, Li G, Nie X, *et al.* Systematic approach to In-Depth understanding of photoelectrocatalytic bacterial inactivation mechanisms by tracking the decomposed building blocks. *Environ Sci Technol.* 2014;48(16):9412-9419.

doi: 10.1021/es502471h

29. Wang F, Li M, Zhang Z, *et al.* Dopamine-perylene diimide polymer with a donor–acceptor structure enhance interfacial electric field for improved H2O2 photosynthesis. *Appl Catal B Environ*. 2025;366:125057.

doi: 10.1016/j.apcatb.2025.125057

30. Ren X, Mao M, Feng M, Peng T, Long X, Yang F. Fate, abundance and ecological risks of microcystins in aquatic environment: The implication of microplastics. *Water Res*. 2024;251:121121.

doi: 10.1016/j.watres.2024.121121

31. Zhou X, Zhou Y, Zhao S, *et al.* Precise MO-FE Dual-Atom coordination regulates the selective generation of Non-Free radicals in peroxymoncosulfate activation. *Adv Funct Mater.* 2025;36(2).

doi: 10.1002/adfm.202513232

32. Li Y, Zhang X, Hou W, *et al.* Tailoring hole-trapping heterojunctions via carbon quantum dot for efficient photocatalytic urea synthesis. *Appl Catal B Environ.* 2025;380:125758.

doi: 10.1016/j.apcatb.2025.125758

33. Sha H, Li J, Wang L, Nong H, Wang G, Zeng T. Preparation of phosphorus-modified biochar for the immobilization of heavy metals in typical lead-zinc contaminated mining soil: Performance, mechanism and microbial community. *Environ Res*. 2022;218:114769.

doi: 10.1016/j.envres.2022.114769

34. Zhao Y, Yang D, Yu C, Yan H. A review on photocatalytic CO2 reduction of g-C3N4 and g-C3N4-based photocatalysts modified by CQDs. *J Environ Chem Eng.* 2025;13(2):115348.

doi: 10.1016/j.jece.2025.115348

35. Shen C, Sun K, Yang Y, Liu C, Liu Y, Wang X. Photoreductive elimination of heavy metal ions and radionuclides by g-C3N4-based materials: A review. *Sep Purif Technol.* 2025;363:132023.

doi: 10.1016/j.seppur.2025.132023

36. Huang B, Xu K, Zhao Y *et al.* Review of the versatility and application potentials of g-C3N4-Based S-Scheme heterojunctions in photocatalytic antibiotic degradation. *Molecules*. 2025;30(6):1240.

doi: 10.3390/molecules30061240

37. Rao J, Cheng Z, Lv H *et al.* Structure design of g-C3N4 based photocatalysis and its application in water splitting: A review. *Diam Relat Mater.* 2025;157:112478.

doi: 10.1016/j.diamond.2025.112478

38. Hayat A, Sohail M, Ajmal Z, *et al.* Advances/Scope and prospects of g-C3N4 derived fascinating photocatalyst as a leading route towards solar energy adaption. *J Clean Prod*. 2024;438:140568.

doi: 10.1016/j.jclepro.2024.140568

39. Lu Y, Hu X, Tang L, *et al.* Effect of CuO/ZnO/FTO electrode properties on the performance of a photo-microbial fuel cell sensor for the detection of heavy metals. *Chemosphere*. 2022;302:134779.

doi: 10.1016/j.chemosphere.2022.134779

40. Tang R, Zeng H, Feng C *et al.* C-TiO2/PCN S-scheme heterojunction with enhanced n→ π* electronic excitation for promoted piezo-photocatalytic effect. *Small*. 2023;19(18):2207636.

doi: 10.1002/smll.202207636

41. Li S, Wang J, Cai X, *et al.* From amorphous to ordered: Ammonia-mediated structural evolution in melon-based carbon nitride photocatalyst. *Appl Catal B Environ.* 2025;381:125807.

doi: 10.1016/j.apcatb.2025.125807

42. Sun J, Wang G. Achieving near infrared photodegradation by the synergistic effect of Z-Scheme heterojunction and antenna of rare Earth single atoms. *Small*. 2025;21(10):e2412148.

doi: 10.1002/smll.202412148

43. Zhang M, Zhang Y, Tang L, *et al.* Ultrathin Bi2WO6 nanosheets loaded g-C3N4 quantum dots: A direct Z-scheme photocatalyst with enhanced photocatalytic activity towards degradation of organic pollutants under wide spectrum light irradiation. *J Colloid Interface Sci.* 2019;539:654-664.

doi: 10.1016/j.jcis.2018.12.112

44. Ong WJ, Tan LL, Ng YH, Yong ST, Chai SP. Graphitic carbon nitride (g-C3N4)-based photocatalysts for artificial photosynthesis and environmental remediation: are we a step closer to achieving sustainability? *Chem Rev.* 2016;116(12):7159-7329.

doi: 10.1021/acs.chemrev.6b00075

45. Mamun AA, Chowdhury AH, Billah A, *et al.* Advancing

Transition Metal Oxide Photoelectrodes for Efficient Solar-Driven Hydrogen Generation: Strategies and Insights. *Adv Energy Mater.* 2025;15(32).

doi: 10.1002/aenm.202501766

46. Fu B, Pan Y, Zhao P, *et al.* "Edge in-situ heterogeneous" BiOI based on defect engineering and non-noble metal deposition: Boosting visible-light photocatalytic sterilization. *Chem Eng J.* 2024;491:152071.

doi: 10.1016/j.cej.2024.152071

47. Liu X, Zhou Y, Yin H, Li X, Duan J. Synergistic Application of PEC-OPECT-CL Multimodal Biosensing and Photocatalytic Sterilization Based on Hollow Tubular Bi12O17Cl2/In2O3 Z-Scheme Heterojunction for Vibrio parahaemolyticus. *J Hazard Mater.* 2025:140831.

doi: 10.1016/j.jhazmat.2025.140831

48. Tan J, Dai Z, Zhou K, Zhang L, Zhou X, Tan Y. Ultrasensitive Screening of Endocrine-Disrupting Chemicals Using a Surface Plasmon Resonance Biosensor with Polarization-Compensated Laser Heterodyne Feedback. *Anal Chem.* 2023;95(22):8687-8695.

doi: 10.1021/acs.analchem.3c01292

49. Li B, Li B, Han Y, *et al.* Rational design of porphyrin-based ionophores for enhanced perchlorate selectivity in ion selective electrodes: application to fireworks wastewater analysis. *Energy Amp Environ Nexus* 2025;1(1):0.

doi: 10.48130/een-0025-0007

50. Zhou C, Yu H, Yang M, Dong XT, Yang Y. CdS/BiOBr Photocatalysts Modified with Monocrystalline Cd Quantum Dots for Sterilization and Degradation of Organic Dyes and Antibiotics. *ACS Appl Nano Mater.* 2025;8(25):12828-12839.

doi: 10.1021/acsanm.5c00732

51. Zhang Y, Wang C, Yin R, *et al.* AgNPs as efficient co-catalysts significantly improve the photocatalytic and antibacterial activities of NaTaO3 nanofilms. *Mater Sci Semicond Processing.* 2023;166:107738.

doi: 10.1016/j.mssp.2023.107738

52. Wang F, Zhan S, Zhou F *et al.* In-situ synthesis of Bi0 on 3D-3D-shaped (BiO) 2CO3 surface for photocatalytic inactivation: Metal self-doping mechanism. *J Environ Chem Eng.* 2022;10(3):107576.

doi: 10.1016/j.jece.2022.107576

53. Zhang C, Song Y, He Q, Wang F, Zhan S, Zhou F. H2O2-assisted photocatalysis induced by SPR of BiQDs anchored on BiVO4 for the production of hydroxyl radicals in seawater. *J Environ Chem Eng.* 2021;9(5):105973.

doi: 10.1016/j.jece.2021.105973

54. Wang F, Zhou F, Zhan S, *et al.* Morphology modulation and performance optimization of nanopetal-based Ag-modified Bi2O2CO3 as an inactivating photocatalytic material. *Environ Res.* 2021;198:111256.

doi: 10.1016/j.envres.2021.111256

55. Sun L, Li W, Lv G, Wang W, Chen S. Strategy for reducing the carriers transfer antagonistic effect between heterojunction and plasmonic effect and weakening photocorrosion of Cu2O for excellent photocatalytic bacteriostasis. *J Colloid Interface Sci.* 2022;630(Pt A):556-572.

doi: 10.1016/j.jcis.2022.10.016

56. Yuan M, Xue J, Li J, Ma S, Wang M. PCN-222/Ag2O-Ag p-n heterojunction modified fabric as recyclable photocatalytic platform for boosting bacteria inactivation and organic pollutant degradation. *Colloids Surf A Physicochem Eng Asp.* 2022;656:130474.

doi: 10.1016/j.colsurfa.2022.130474

57. Xiao W, Huang Z, Tang Y, Li Y, Situ W, Song X. Effect of nano-Ag proportion on the structure of Ag– TiO2–Bi2WO6 photocatalyst and its antibacterial property on Escherichia coli. *Opt Mater.* 2023;137:113539.

doi: 10.1016/j.optmat.2023.113539

58. Qin Y, Guo Y, Liang Z, *et al.* Au nanorods decorated TiO2 nanobelts with enhanced full solar spectrum photocatalytic antibacterial activity and the sterilization file cabinet application. *Chin Chem Lett.* 2020;32(4):1523-1526.

doi: 10.1016/j.cclet.2020.10.020

59. Pulliam JR. Lower infection rates after introduction of a photocatalytic surface coating. *Am J Infect Control.* 2014;43(2):180-181.

doi: 10.1016/j.ajic.2014.10.023

60. Zhang M, Zhang Y, Zhang Y, *et al.* Synergetic utilization of 3D materials merits and unidirectional electrons transfer of Schottky junction for optimizing optical absorption and charge kinetics. *Appl Catal B Environ.* 2021;295:120278.

doi: 10.1016/j.apcatb.2021.120278

61. Li D, Wen Q, Gao C *et al.* Schottky Junction and D–A1–A2 System Dual Regulation of Graphite-Phase Carbon Nitride for Piezo-Photocatalytic H2O2 Production. *Small.* 2025;21(25):2500797.

doi: 10.1002/smll.202500797

62. Guo H, Niu HY, Wang WJ, *et al.* Schottky barrier height mediated Ti3C2 MXene based heterostructure for rapid photocatalytic water disinfection: Antibacterial efficiency and reaction mechanism. *Sep Purif Technol.* 2023;312:123412.

doi: 10.1016/j.seppur.2023.123412

63. Tahir B, Alraeesi A, Tahir M. Bimetallic Au–Co-assisted exfoliated g-C3N4 nanosheets with dual sites for plasmon-induced photocatalytic solar H2 production. *Int J Hydrog Energy.* 2025;136:1061-1072.

doi: 10.1016/j.ijhydene.2025.04.304

64. Bai S, Jiang J, Zhang Q, Xiong Y. Steering charge kinetics in photocatalysis: intersection of materials syntheses, characterization techniques and theoretical simulations. *Chem Soc Rev.* 2015;44(10):2893-939.

doi: 10.1039/C5CS00064E

65. He S, Huang J, Goodsell JL, Angerhofer A, Wei WD. Plasmonic Nickel–TiO2 heterostructures for visible-light-driven photochemical reactions. *Angew Chem Int Ed.* 2019;58(18):6038-6041.

doi: 10.1002/anie.201901987

66. Naldoni A, Guler U, Wang Z, *et al.* Broadband Hot-Electron Collection for Solar Water Splitting with Plasmonic Titanium Nitride. *Adv Opt Mater.* 2017;5(15).

doi: 10.1002/adom.201601031

67. Macchia E, Di Franco C, Scandurra C, *et al.* Plasmonic Single-Molecule affinity detection at 10 −20 molar. *Adv Mater.* 2025;37(9):e2418610.

doi: 10.1002/adma.202418610

68. Tong F, Liang X, Bao X, Zheng Z. Photocatalysis on hybrid plasmonic nanomaterials: From catalytic mechanism study at Single-Particle Level to materials design. *ACS Catal.* 2024;14(15):11425-11446.

doi: 10.1021/acscatal.4c03566

69. Yan T, Su M, Wang Z, Zhang J. Second near-infrared plasmonic nanomaterials for photoacoustic imaging and photothermal therapy. *Small.* 2023;19(30):2300539.

doi: 10.1002/smll.202300539

70. Xu X, Dutta A, Khurgin J, Wei A, Shalaev VM, Boltasseva A. TiN@ TiO2 core–shell nanoparticles as plasmon-enhanced photosensitizers: the role of hot electron Injection. *Laser Photonics Rev.* 2020;14(5):1900376.

doi: 10.1002/lpor.202070031

71. Koya AN, Zhu X, Ohannesian N *et al.* Nanoporous metals: From plasmonic properties to applications in enhanced spectroscopy and photocatalysis. *ACS Nano.* 2021;15(4):6038-6060.

doi: 10.1021/acsnano.0c10945

72. Wang M, Chen D, Lu J. Recent advances in the construction of structurally diverse catalysts for enhanced photocatalytic CO2 reduction. *Sep Purif Technol.* 2024;343:126917.

doi: 10.1016/j.seppur.2024.126917

73. Han C, Quan Q, Chen HM, Sun Y, Xu Y. Progressive Design of Plasmonic Metal–Semiconductor Ensemble toward Regulated Charge Flow and Improved Vis–NIR-Driven Solar-to-Chemical Conversion. *Small.* 2017;13(14).

doi: 10.1002/smll.201602947

74. Zhang M, Tang L, Duan A *et al.* Adjusting charge kinetics of conjugated polymers via integration of LSPR effect with homojunction. *Chem Eng J.* 2022;452:139068.

doi: 10.1016/j.cej.2022.139068

75. Zhang L, Ding N, Lou L *et al.* Localized surface plasmon resonance enhanced photocatalytic hydrogen evolution via Pt@ Au NRs/C3N4 nanotubes under visible-light irradiation. *Adv Funct Mater.* 2019;29(3):1806774.

doi: 10.1002/adfm.201806774